Published in "Nature Physics 8: 331–337 , 2012"
which should be cited to refer to this work.

Satellites and large doping and temperature dependence of electronic properties in hole-doped $BaFe_2As_2$

Philipp Werner[1,2]★, Michele Casula[3], Takashi Miyake[4,5,6], Ferdi Aryasetiawan[7,8], Andrew J. Millis[9] and Silke Biermann[5,10]

Superconductivity has recently been discovered in several families of iron-based compounds, but despite intense research even such basic electronic properties of these materials as Fermi surfaces, effective electron masses and orbital characters are still subject to debate. Here, we address an issue that has not been considered before, namely the consequences of dynamical screening of the Coulomb interactions between Fe *d* electrons. We demonstrate that dynamical screening effects are important not only for higher-energy spectral features, such as correlation satellites seen in photoemission spectroscopy, but also for the low-energy electronic structure. Our analysis indicates that $BaFe_2As_2$ is a strongly correlated compound with strongly doping- and temperature-dependent properties. In the hole-overdoped regime an incoherent metal is found, whereas Fermi-liquid behaviour is recovered in the undoped compound. At optimal doping, the self-energy exhibits an unusual square-root energy dependence, which leads to strong band renormalizations near the Fermi level.

Known superconductors can be assigned to one of two classes: for 'weakly correlated' materials such as MgB_2 one-electron theories describe the basic electronic properties well and the superconducting pairing mechanism has been understood in this framework in terms of the interaction between electrons and quantum fluctuations of the lattice. Materials of the second, 'strongly correlated' class exhibit sometimes spectacular inconsistencies with the one-electron picture, leaving unclear even the theoretical language in which a theory of the pairing mechanism should be formulated. High-transition-temperature (high-T_c) cuprate superconductors fall in this category. The role of electronic correlations in the recently discovered iron-based high-T_c superconductors[1] apparently depends on the specific family, as well as on doping, substitutions or pressure. In this work, we address the prototypical compound of the so-called 122 family, $BaFe_2As_2$, which exhibits superconductivity under pressure[2,3] or under hole as well as electron doping[4,5]. Many experimental probes, including angle-resolved and angle-integrated photoemission spectroscopy[6–12], optics and transport, Raman and neutron scattering and nuclear magnetic resonance, have been employed to characterize the electronic properties[13]. The Fermi surface consists of two concentric hole pockets around the Brillouin zone centre (Γ point), and elliptic electron pockets around the zone face (M; ref. 14). Experimental estimates of the mass enhancements vary substantially with doping; literature values range from about 1.4 to 5, at least for the orbital pointing towards the As sites[15,16]. The orbital character of these pockets is still subject to debate, but there seems to emerge a consensus about stronger correlation effects for holes than electrons.

Understanding the low-energy electronic structure, in particular Fermi surface nesting, orbital character and mass enhancements, is a prerequisite for assessing possible pairing mechanisms[13,17–19]. The field of electronic structure calculations for correlated materials has made tremendous progress in recent years, most notably thanks to the combination of electronic structure and many-body techniques. The combined 'DFT + DMFT' scheme builds on density functional theory (DFT) to construct realistic many-body Hamiltonians, which are solved using dynamical mean-field theory (DMFT; refs 20–22). Although a number of interesting applications of this scheme to iron pnictides (see for example refs 23–25) have emerged, it has become clear that one of the bottlenecks is the determination of the Coulomb matrix elements ('Hubbard parameters' U and J), which parameterize the energetic cost associated with the distribution of electrons among the localized Fe d orbitals. Recent works try to extract these values from constrained density functional calculations[23], GW-inspired methods[26] or random-phase-approximation (RPA)-based schemes. All these calculations result in interaction parameters that are strongly reduced from the corresponding atomic values through screening from other degrees of freedom in the solid. As is clearly seen in the constrained RPA approach[27], the screening implies that the 'Hubbard U' for the Fe d electrons acquires a frequency dependence. However, the dynamical nature of the effective Coulomb interactions has heretofore not been treated at the level

[1]Department of Physics, University of Fribourg, 1700 Fribourg, Switzerland, [2]Theoretische Physik, ETH Zurich, 8093 Zürich, Switzerland, [3]CNRS and Institut de Minéralogie et de Physique des Milieux Condensés, Université Pierre et Marie Curie, case 115, 4 place Jussieu, 75252, Paris cedex 05, France, [4]Nanosystem Research Institute (NRI) RICS, AIST, Tsukuba, Ibaraki 305-8568, Japan, [5]Japan Science and Technology Agency, CREST, Kawaguchi, Saitama 332-0012, Japan, [6]Japan Science and Technology Agency, TRIP, Chiyoda, Tokyo 102-0075, Japan, [7]Department of Physics, Mathematical Physics, Lund University, Sölvegatan 14A, 223 62 Lund, Sweden, [8]Graduate School of Advanced Integration Science, Chiba University, Chiba 263-8522, Japan, [9]Department of Physics, Columbia University, 538 West 120th Street, New York, New York 10027, USA, [10]Centre de Physique Théorique, Ecole Polytechnique, CNRS-UMR7644, 91128 Palaiseau, France. *e-mail: philipp.werner@unifr.ch.

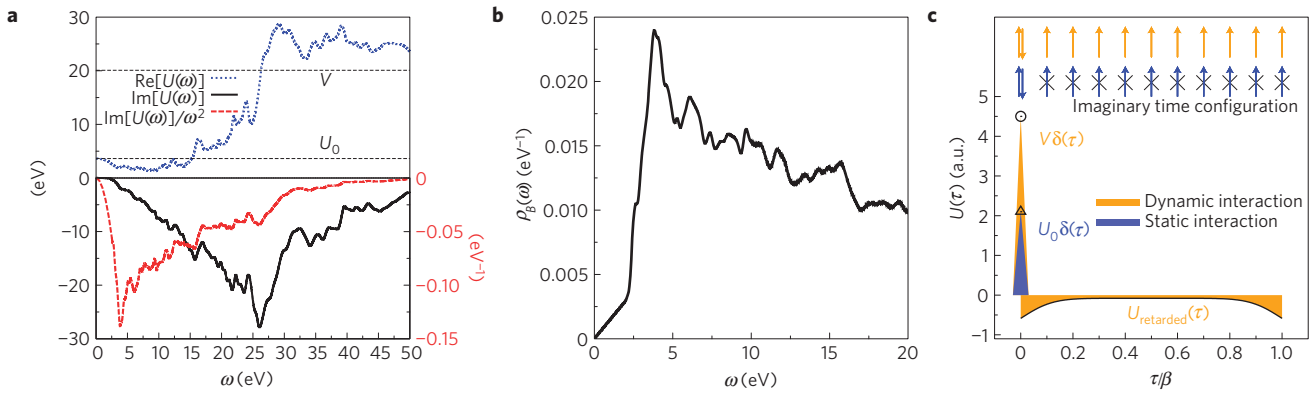

Figure 1 | Frequency-dependent interaction for $BaFe_2As_2$ from constrained RPA. a, Real and imaginary parts of the average intra-orbital Coulomb interaction as a function of frequency. V is the unscreened (bare) Coulomb interaction and U_0 the static (partially screened) interaction. $\mathrm{Im}U(\omega)/\omega^2$, plotted as a red line, features prominent peaks at 3.8 eV, 6.1 eV, 16 eV and 26 eV, and smaller humps at 10 eV and 12 eV. **b**, Spectral function of the bosonic propagator B. The peaks of this function, inherited from the structures in $\mathrm{Im}U(\omega)/\omega^2$, determine the energies of satellite structures in the d-electron density of states. **c**, A schematic plot illustrating the difference between a static-U (blue) and a dynamic-U (yellow) calculation. In a static-U calculation, up-spin and down-spin electrons interact locally in time with the partially screened Coulomb interaction U_0. In the dynamic-U calculation, the instantaneous interaction is given by the bare V, whereas screening effects lead to an attractive retarded interaction $U_{\mathrm{retarded}}(\tau)$.

of the actual many-body calculation. In this paper we demonstrate the importance of the frequency dependence for the low-energy electronic structure, in particular quasiparticle mass enhancements and lifetimes, as well as for the theoretical description of the correlation satellites seen in photoemission spectroscopy.

Partially screened Coulomb interaction

The constrained RPA result for the average intra-orbital Coulomb repulsion U of $BaFe_2As_2$ has been obtained as described in Supplementary Information and is shown in Fig. 1a. $U(\omega)$ represents a partially screened Coulomb interaction for the Fe d states, which accounts for screening by all degrees of freedom except the Fe d states themselves. The real part ranges from the static value $U_0 \equiv \mathrm{Re}U(\omega=0) = 3.6$ eV to the bare interaction V of about 20 eV at large ω, and the frequency dependence resembles typical $U(\omega)$ in transition metals[27,28]. Screening does not arise from a well-defined plasmon excitation. Instead, $\mathrm{Im}U(\omega)$ is characterized by a broad structure beginning from a peak at ~ 26 eV and extending down to a few eV, implying that any plasmon excitations overlap strongly with the one-particle excitations, a reflection of the semi-itinerant nature of the Fe 3d electrons. Fourier transformation yields a time-dependent Hubbard interaction term $\int\int \mathrm{d}\tau \mathrm{d}\tau' N(\tau) U(\tau-\tau') N(\tau')$, with $U(\tau) = V\delta(\tau) + U_{\mathrm{retarded}}(\tau)$, which describes the local Coulomb interaction including retardation effects due to quantum fluctuations that screen the bare V (Fig. 1c and Methods section).

In a standard DFT + DMFT calculation without dynamical effects, the relatively small value we find for the interaction U_0 would result in a rather weakly correlated picture. This is demonstrated in Fig. 2b, which presents the Fe d spectral function obtained by using our computed U_0 in a standard DFT + DMFT calculation. Interaction effects lead to a moderate renormalization of the Fe d states, with a mass enhancement of 1.6. A comparison with the DFT density of states in Fig. 2a shows that the peaks at -3 eV and 1 eV are weakly renormalized band states. No Hubbard satellites or other correlation features appear, in agreement with previous studies[23,29].

The new aspect of our work, compared with previous simulations, is the treatment of the full frequency dependence of the interaction. In refs 30,31 it was shown in the context of simple model calculations how a frequency-dependent interaction can be incorporated efficiently into quantum Monte Carlo simulations within the hybridization expansion impurity solver scheme[32]. Here, we generalize this technique to multiorbital systems and realistic materials. The effect of $U(\omega)$ is to dress the fermionic propagators with a bosonic propagator

$$B(\tau) = \exp[-K(\tau)] \qquad (1)$$

where $K(\tau)$ is the twice-integrated retarded interaction. In terms of $\mathrm{Im}U(\omega)$ and a factor $b(\tau,\omega) = \cosh[(\tau-(\beta/2))\omega]/\sinh[\beta\omega/2]$ with bosonic symmetry, we can write[31]

$$K(\tau) = \int_0^\infty \frac{\mathrm{d}\omega}{\pi} \frac{\mathrm{Im}U(\omega)}{\omega^2}[b(\tau,\omega) - b(0,\omega)] \qquad (2)$$

It is evident from equation (2) that, as far as structures in the frequency-dependent interaction are concerned, the relevant function to analyse is $\mathrm{Im}U(\omega)/\omega^2$. This function is plotted as the red dashed line in Fig. 1a. In addition to a first peak at 3.8 eV, which comes from the rapid decay of $\mathrm{Im}U(\omega)$ at small frequencies, there are prominent peaks at 6.1 eV, 16 eV and 26 eV, as well as smaller features at 10 eV and 12 eV. We have traced the origin of the 6.1 eV feature to transitions from occupied d states to states in the energy window [6 eV : 7 eV], which have predominantly Ba character.

Spectral functions and high-energy satellites

As explained in ref. 33 and in Supplementary Information, we compute the electron spectral function as the convolution of the spectral function $\rho_B(\omega)$ of the bosonic propagator $B(\tau)$ defined in equation (1) and the spectral function $\rho_{\mathrm{aux}}(\omega)$ of the auxiliary Green function $G_{\mathrm{auxiliary}}(\tau) = G(\tau)/B(\tau)$ (Supplementary Equation (S9)). For systems with a single well-defined plasma frequency the effect of this convolution would be to replicate the low-energy spectral features of $\rho_{\mathrm{aux}}(\omega)$, with exponentially decreasing weights, displaced by multiples of the plasma frequency. These satellites correspond to processes where in addition to the one-electron addition or removal process a certain number of plasmons are emitted or absorbed. In the present case, the bosonic spectrum, plotted in Fig. 1b, is more complex than just a single plasmon delta-function, because it inherits the structures of $\mathrm{Im}U(\omega)/\omega^2$. Nevertheless, sharp features present in $\rho_B(\omega)$ lead to replications of the structure of the low-energy spectral density and thus to dispersionless satellite features in the photoemission spectrum.

The low-energy part of the d-electron spectral function from the dynamic-U calculation is shown in Fig. 2b, and the total spectral function (p and d contributions) in Fig. 2c. In the dynamic-U calculation, spectral weight is shifted to high energies, which leads

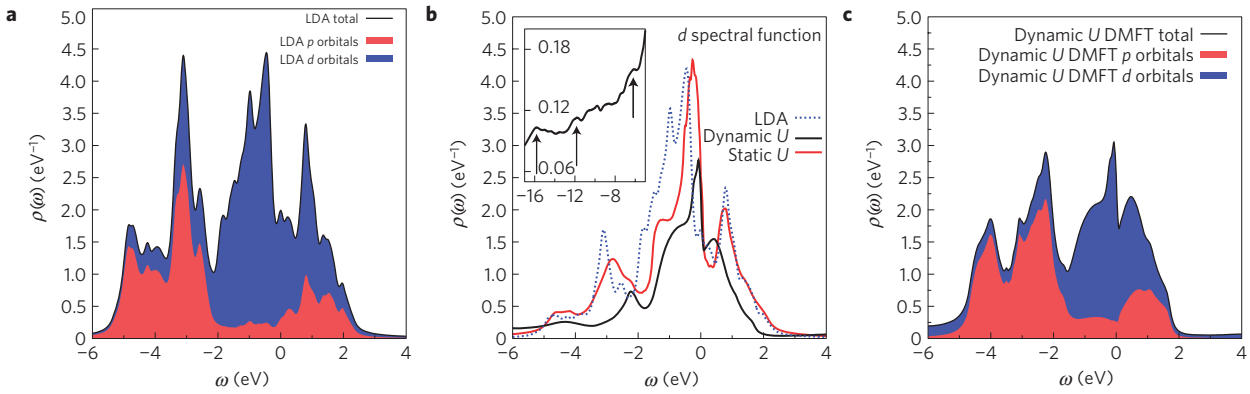

Figure 2 | Effect of $U(\omega)$ on the d-electron spectral function. a, Total LDA density of states for $BaFe_2As_2$ with the p- and d-electron contributions shaded in red and blue, respectively. **b**, d-electron spectral function obtained from the DMFT calculation at $T = 290$ K and optimal hole doping ($x = 0.2$ per Fe), using the static value U_0 (red curve) and the full frequency-dependent $U(\omega)$ (black curve). The inset shows the high-energy tail of the d-electron spectral function. Arrows indicate the positions of satellites predicted by the dynamic-U calculation. **c**, Total spectral function (p and d contributions) of optimally doped $BaFe_2As_2$ obtained from DMFT.

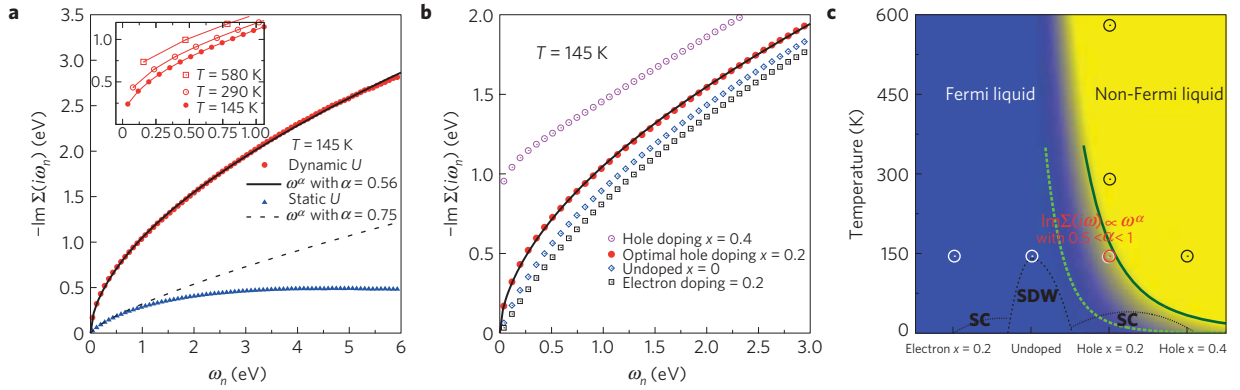

Figure 3 | NFL behaviour of the self-energy. a, Imaginary part of the self-energy (orbital average) on the Matsubara axis for optimal hole doping ($x = 0.2$ per Fe), for both the dynamic-U calculation (red circles) and the static-U calculation (blue triangles). Solid and dashed lines are fits of the low-frequency behaviour to the function $-\mathrm{Im}\Sigma(i\omega_n) = A(\omega_n)^\alpha$. The inset shows the low-frequency behaviour of the dynamic-U result for different temperatures. As the temperature is raised, the extrapolation $\omega_n \to 0$ yields a non-zero intercept, which indicates that even excitations at the Fermi level exhibit a finite lifetime. **b**, Low-energy behaviour of the self-energy as a function of doping. Fermi-liquid behaviour is found in the undoped and electron-doped compounds, whereas a non-zero intercept appears in the overdoped case. **c**, Sketch of the phase diagram in the space of temperature and doping. The blue region indicates Fermi-liquid behaviour, whereas yellow indicates a frequency dependence of the self-energy that is not compatible with Fermi-liquid theory. The light green dashed line marks the boundary of the crossover region, where the exponent α starts to deviate from 1. The dark green solid line corresponds to $\alpha = 0.5$, which marks the 'spin-freezing' transition. To the right of this line, an incoherent metal phase with non-zero intercept of $\mathrm{Im}\Sigma$ is found. The experimentally measured phase diagram with superconducting (SC) and spin-density-wave (SDW) ordered phases is indicated by black dotted lines. Full substitution (KFe_2As_2) corresponds to $x = 0.5$.

to a reduction in weight at low energies, compared with the static-U result. More importantly, we see that the structures arising from p–d hybridization are shifted closer to the Fermi energy, and the peak near $\omega = 0$ is strongly renormalized. Thus, the explicit treatment of the strong Coulomb repulsion at large frequencies has a substantial effect, even on the low-energy properties of the system. The large quantitative effect of $U(\omega)$ is remarkable given the fact that the real part of the frequency-dependent interaction (Fig. 1a) remains of the order of U_0 or lower up to $\omega \sim 15$ eV.

The sharp low-energy peak in the d-electron spectral function results in weak but well-defined satellites, as discussed above. The inset of Fig. 2b shows the high-energy tail of the occupied part of the spectrum, with arrows marking the most prominent satellites at -6.1 eV, -12 eV and -16 eV. This physics is not contained in a static-U calculation or any other previous theoretical work on pnictides. The observation of satellites at -6.5 eV and -12 eV was emphasized in the photoemission study of ref. 8. Whereas ref. 34 confirms a hump in the d-electron spectral function around -6.5 eV, these authors suggest that the feature at -12 eV is an As 4s line. Our calculation suggests that a d feature, originating from the structure in the frequency-dependent interaction, is superimposed on the As 4s spectral contribution. The -16 eV feature is probably not visible in experiments, because it overlaps with Ba 5p states, whereas a satellite that we predict at -3.8 eV is masked by structures arising from p–d hybridization.

Non-Fermi-liquid properties of the metallic phase

Our theoretical study predicts unusual non-Fermi-liquid (NFL) properties of the metallic phase near optimal doping, which lead to a sensitive doping and temperature dependence of the low-energy electronic structure. In a Fermi liquid, the imaginary part of the Matsubara axis self-energy exhibits a linear regime at low energy, whose slope is directly related to the quasiparticle mass enhancement. However, as shown in Fig. 3a, for optimally doped $BaFe_2As_2$ ($x = 0.2$ hole doping per Fe), and at the temperatures of our simulations, we do not observe this behaviour:

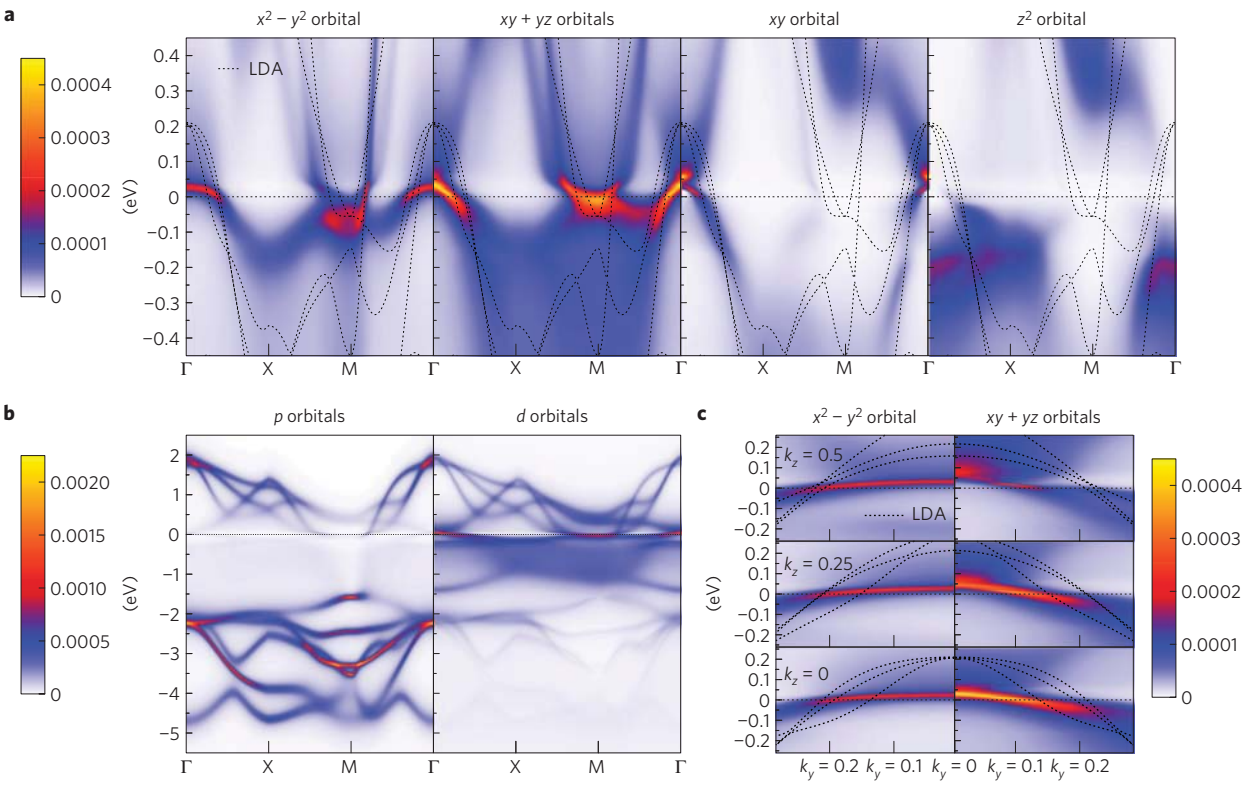

Figure 4 | Orbitally resolved spectral functions for optimally doped $BaFe_2As_2$ at $T = 145$ K. a, Spectral functions along the path Γ–X–M–Γ, comparing the DMFT result with LDA calculations (dotted). The bands are strongly renormalized near the Fermi energy. **b**, Total *p* and *d* contributions to the spectral function in a wide energy window. The *p* states hybridize with the *d* states mainly in the unoccupied part of the spectrum. This is because it is precisely this hybridization that pushes the *d* states up in energy. **c**, Cut through the hole pocket near $(k_x, k_y) = (0, 0)$, for different values of k_z from Γ to Z, and resolved into $x^2 - y^2$ and $xy + yz$ contributions. Dotted lines indicate the LDA bands.

the self-energy behaves as $-\mathrm{Im}\Sigma(i\omega_n) = A(i\omega_n)^\alpha$ with $\alpha \approx 0.56$ at temperature $T = 145$ K, whereas a frequency dependence of the form $-\mathrm{Im}\Sigma(i\omega_n) = C + A(i\omega_n)^\alpha$, with non-zero intercept (scattering rate) C is found at $T = 290$ K and $T = 580$ K.

A similar phenomenon has recently been observed in the metallic phase of a three-orbital model[35], and has been dubbed a 'spin-freezing' transition, because the intercept C is due to scattering off static (but disordered) local moments. The exponent value $\alpha = 0.5$ (and simultaneous onset of an intercept $C > 0$) mark the transition into the spin-frozen or incoherent metal regime. Large deviations from Fermi-liquid behaviour thus appear in the vicinity of this transition. The phenomena described in ref. 35 are a generic property of the metallic phase in multiorbital systems with large Hund coupling. Our results in Fig. 3a indicate that optimally doped $BaFe_2As_2$ at $T \approx 150$ K is close to the spin-freezing transition, and that increasing the temperature shifts the material across the spin-freezing boundary into the incoherent metal regime.

The sublinear frequency dependence of the self-energy means that Landau quasiparticles and effective masses cannot be properly defined and further implies that the bands very close to the Fermi level are much more strongly renormalized than those further away, consistent with the behaviour seen in Fig. 2. This NFL property may explain why different photoemission experiments arrive at considerably different estimates for band renormalizations, and why it has been so difficult to reach a consensus on the importance of correlations in $BaFe_2As_2$ (and, possibly, other pnictides).

Whereas Fermi-liquid properties may eventually be recovered in simulations at low enough temperature (Fig. 3c), such behaviour is cut off in real materials by the onset of the spin-density-wave or superconducting phase. Thus the NFL and incoherent metal regime dominates the physics in the whole temperature range of relevance to this study. We also note that NFL behaviour has been proposed for LaFeAsO and FeSe, on the basis of static-U calculations[36–38]. Figure 3a shows the self-energy obtained by using a static U with a value equal to the zero-frequency screened U. Comparison with the dynamic-U calculations shows that the static-U approximation underestimates the departures from Fermi-liquid behaviour: fitting the self-energy to $\mathrm{Im}\Sigma(i\omega_n) = A(i\omega_n)^\alpha$ yields $\alpha \approx 0.75$, which is much closer to Fermi-liquid behaviour. Properly including the frequency dependence of U leads to a substantially enhanced self-energy, and a much larger frequency range over which the NFL exponent describes the self-energy. In this sense, the dynamic-U calculation, by increasing the interaction effects, shifts the material closer to the spin-freezing transition, and the proximity to this transition line results in a sensitive dependence on parameters such as temperature and doping level.

Figure 3b shows the low-energy part of the self-energy of $BaFe_2As_2$ at $T = 145$ K for different dopings. Increasing the hole doping leads to a large scattering rate whereas reducing the doping leads to a coherent Fermi-liquid state with modest mass enhancement and minimal many-body scattering. For undoped and 20% electron-doped materials we find a Fermi-liquid behaviour at the lowest temperatures, with orbitally averaged mass renormalization factors 2.6 and 1.8 respectively. In the hole-doped regime the proximity to the spin-freezing transition means that the renormalization of the bands depends on the distance from the Fermi energy, and only an approximate 'mass enhancement' can be computed. Using the usual estimate based on the derivative of $\mathrm{Im}\Sigma$ evaluated at the lowest Matsubara frequency, we find at optimal doping ($x = 0.2$) the values 4.35 at $T = 145$ K or 3.95 at $T = 290$ K, in quite good agreement with the mass enhancement of about 5 deduced from specific-heat measurements[39].

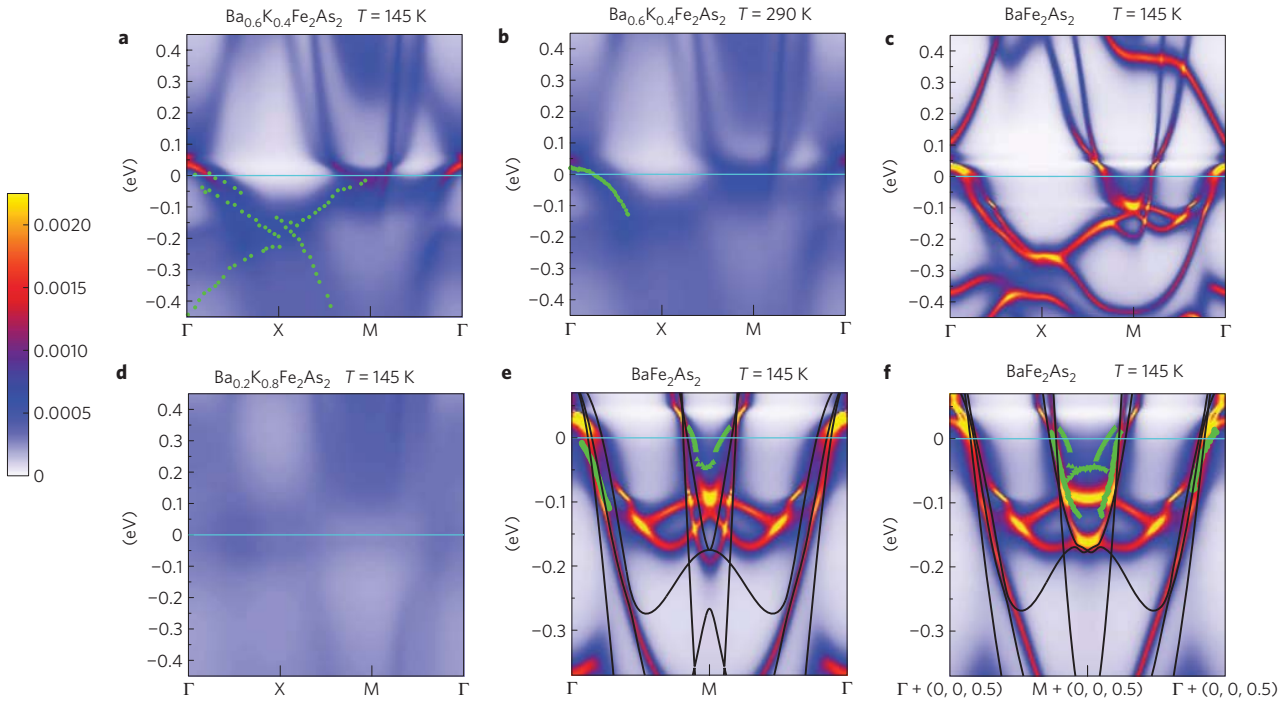

Figure 5 | Doping and temperature dependence of the low-energy spectral functions, and comparison with photoemission experiments. **a**,**b**, Renormalized band structure at optimal doping ($x = 0.2$) and comparison with photoemission data taken from ref. 8 (green symbols). We plot the result for two temperatures, $T = 145$ K (**a**) and $T = 290$ K (**b**), to illustrate the smearing of the bands at elevated temperature. **c**,**d**, Doping dependence of the renormalized band structure. The undoped compound is in the moderately correlated Fermi-liquid regime, whereas the overdoped compound ($x = 0.4$) is in the incoherent metal regime, where the scattering off static moments washes out the bands. **e**,**f**, Simulation results for the undoped compound at $T = 145$ K, and comparison with photoemission data from ref. 16 (green symbols) and the LDA band structure (lines).

Our results on the NFL behaviour are summarized in Fig. 3c, which sketches the phase diagram in the space of temperature and doping. The incoherent metal regime is shown in yellow, and the Fermi-liquid region in blue. The solid green line is defined by the power-law exponent $\alpha = 0.5$ (with simultaneous onset of static magnetic moments) and represents the boundary of the spin-frozen region in the sense of ref. 35. The dashed green line marks the temperature and doping level below which Fermi-liquid behaviour is recovered.

Momentum-resolved spectral functions

Spectral functions for optimally doped $BaFe_2As_2$ are shown in Fig. 4. The orbitally resolved d-electron spectral functions along the path Γ–X–M–Γ are plotted in a narrow energy range in Fig. 4a. A comparison with the original local density approximation (LDA) band structure (dotted lines) shows the strong band renormalization at low energies, a consequence of the 'square root' behaviour of the self-energy near the spin-freezing transition. We also see that the z^2 orbital has no weight at the Fermi energy, which at first sight might suggest a simpler model for $BaFe_2As_2$, involving fewer d orbitals. However, owing to the sensitive doping dependence of the spin-freezing phenomenon, such models may have properties that are very different from those of our five-orbital model (in a half-filled four-orbital model, spin freezing occurs only in the vicinity of the Mott insulating phase).

Figure 4b plots the total p and d contributions to the spectral function along the Γ–X–M–Γ path. Remarkably, the p bands (energy range [−5 eV: − 2 eV]) hybridize with the d bands (energy range [−2 eV:2 eV]) mainly in the unoccupied part of the spectrum. This property, which can already be seen at the LDA level[40], is amplified in the DMFT description, because the empty d states are much better defined than the filled states, whose spectra are smeared out by the self-energy effects described above. It may lead to a further asymmetry between electron and hole doping, beyond the strong doping asymmetry implied by the spin-freezing phenomenon.

A close-up view of the hole pocket near Γ is shown for several values of k_z in Fig. 4c. Dotted lines again indicate the LDA bands. Although the renormalization of these bands is very large, the k_z dispersion of the Fermi surface is found to be weak in the DMFT description. The outer Fermi surface has predominantly $x^2 - y^2$ character and the inner Fermi surface $xz + yz$ character.

A comparison of low-energy momentum-resolved spectra with photoemission data is presented in Fig. 5. Figure 5a,b shows the spectral function along the path Γ–X–M–Γ, for optimal hole doping $x = 0.2$, $T = 145$ K (Fig. 5a) and $T = 290$ K (Fig. 5b). Angle-resolved photoemission data from ref. 8 are indicated by green symbols. (The photoemission spectra were measured at $T = 50$ K and $T = 145$ K, respectively.) The agreement near the Γ, X and M points is remarkably good, which shows that the very strong low-energy renormalization implied by the NFL self-energy is consistent with experiment. Increasing the temperature leads to a smearing of the bands, a result of the temperature-dependent intercept of $\mathrm{Im}\Sigma$ shown in the inset of Fig. 3a. Figure 5c,d illustrates the strong doping dependence of the spectra. In Fig. 5c, we show the result for the undoped compound at $T = 145$ K, which is in the Fermi-liquid region of the schematic phase diagram (Fig. 3c). Indeed, our calculation produces well-defined bands with a modest renormalization consistent with the factor 2.6 extracted from the slope of the Matsubara axis self-energy. In Fig. 5d, we plot the spectral function of the overdoped sample ($x = 0.4$), which falls into the incoherent metal phase characterized by a non-zero intercept of $\mathrm{Im}\Sigma$. As a result, the bands are smeared out. We also note that the electron pocket at M has disappeared. These theoretical predictions are consistent with measurements on the end member of the series, KFe_2As_2, reported in refs 41,42. Figure 5e,f compares the low-energy band structure in the undoped compound at $T = 145$ K to

photoemission data taken from ref. 16 (green symbols) and the LDA bands (black lines). In this case, our calculation underestimates the band renormalization somewhat. However, given the large differences in the band renormalizations between the optimally doped and undoped compounds, we consider the agreement with the theoretical calculation satisfactory. We note that the discrepancy with the experiment is less than 0.05 eV, and thus much smaller than in any previous theoretical work.

The spin–spin correlation function is known to exhibit an unusually slow (imaginary time) decay near the spin-freezing transition, whereas there is no particular anomaly in the orbital correlation functions[35]. Whether and how these properties are related to our observation that the maximum superconducting transition temperature in $BaFe_2As_2$ is reached in the vicinity of the spin-freezing transition is an interesting topic for future investigations.

Methods

Our scheme can be viewed as an extension of the combined DFT + DMFT method[21,22] to dynamical interactions, or as promoting extended DMFT[43,44] to a realistic scheme by combining it with input from electronic-structure calculations within the density functional and constrained RPA frameworks. Alternatively, our method can be considered as an approximation to a full GW + DMFT calculation[45]. The present scheme simplifies the general formulation in so far as only a local self-energy is calculated (as in DMFT) and two-particle quantities are calculated at a non-self-consistent level. Thereby practical calculations become feasible even for complex multiband systems such as the iron pnictide compounds.

In a Hamiltonian formulation, we can write the multiorbital model with dynamically screened interactions as

$$\begin{aligned} H &= \sum_{\{im\sigma\}} (H^{\mathrm{LDA}}_{im,i'm'} - H^{\text{double counting}}_{im,i'm'}) a^{\dagger}_{im\sigma} a_{i'm'\sigma} \\ &+ \frac{1}{2} \sum_{\substack{imm'\sigma \\ \text{(correl. orb.)}}} V_{mm'} n_{im\sigma} n_{im'-\sigma} + \frac{1}{2} \sum_{\substack{im\neq m'\sigma \\ \text{(correl. orb.)}}} (V_{mm'} - J_{mm'}) n_{im\sigma} n_{im'\sigma} \\ &+ \sum_i \int \mathrm{d}\omega \Big[\lambda_{i\omega} (b^{\dagger}_{i\omega} + b_{i\omega}) \sum_{m\sigma} n_{im\sigma} + \omega b^{\dagger}_{i\omega} b_{i\omega} \Big] \end{aligned} \tag{3}$$

It consists of a multiorbital Hamiltonian with Slater–Koster interaction parameters V and J, which depend on orbital indices m, m' and are defined as in ref. 22, albeit with the bare Coulomb interaction V entering the Hubbard terms, and a further bosonic Hamiltonian with bosonic modes coupling to the total electronic occupations of the atomic sites. Here, $a^{\dagger}_{im\sigma}$ creates an electron on atom i in orbital m with spin σ and $n_{im\sigma}$ is the number operator for such electrons. For computational reasons, we have restricted ourselves to density–density interactions. The bosonic part of the Hamiltonian describes the coupling of the electronic degrees of freedom (through the total charge $N_i = \sum_{m\sigma} n_{im\sigma}$ on site i and some coupling constant $\lambda_{i\omega}$) to bosonic modes. These bosonic modes represent the screening (through both plasmonic and single-particle excitations of the non-d electrons) of the charge fluctuations on the Fe d sites.

We solve the multiorbital lattice problem using DMFT (ref. 20), which maps it to a self-consistent solution of a five-orbital quantum impurity model. This local approximation, and the integration over the bosonic degrees of freedom, leads to an action of the form

$$\begin{aligned} S_{\mathrm{imp}} &= \iint \mathrm{d}\tau \, \mathrm{d}\tau' \sum_{\substack{mm'\sigma \\ \text{(correl. orb.)}}} a^{\dagger}_{m\sigma}(\tau) \mathcal{G}^{-1}_{0mm'\sigma}(\tau\tau') a_{m'\sigma}(\tau') \\ &+ \frac{1}{2} \int \mathrm{d}\tau \sum_{\substack{mm'\sigma \\ \text{(correl. orb.)}}} V_{mm'} n_{m\sigma}(\tau) n_{m'-\sigma}(\tau) \\ &+ \frac{1}{2} \int \mathrm{d}\tau \sum_{\substack{m\neq m'\sigma \\ \text{(correl. orb.)}}} (V_{mm'} - J_{mm'}) n_{m\sigma}(\tau) n_{m'\sigma}(\tau) \\ &+ \frac{1}{2} \int \mathrm{d}\tau \, \mathrm{d}\tau' N(\tau) U_{\mathrm{retarded}}(\tau - \tau') N(\tau') \end{aligned} \tag{4}$$

with dynamical 'Weiss fields' $\mathcal{G}^{-1}_{0mm'\sigma}$, $-\mathrm{Im}U_{\mathrm{retarded}}(\omega) = \pi\lambda^2_{\omega}$, and the partially screened interaction $U_0 = V - 2\int \mathrm{d}\omega(\lambda^2_{\omega}/\omega)$.

The frequency-dependent (or retarded) U can be viewed as a systematically downfolded interaction, stemming from a static Hamiltonian including all—even high-energy—degrees of freedom, in the sense of ref. 27. In practice, we calculate it from the constrained RPA method as described in Supplementary Information. The impurity model (with frequency-dependent interactions) is solved using a Monte Carlo method based on a stochastic expansion of the partition function in the impurity-bath hybridization[31,32]. Details can be found in Supplementary Information.

Received 11 July 2011; accepted 27 January 2012; published online 4 March 2012

References

1. Kamihara, Y. *et al.* Iron-based layered superconductor $La[O_{1-x}F_x]FeAs$ ($x = 0.05$–0.12) with $T_c = 26$ K. *J. Am. Chem. Soc.* **130,** 3296–3297 (2008).
2. Alireza, P. M. *et al.* Superconductivity up to 29 K in $SrFe_2As_2$ and $BaFe_2As_2$ at high pressures. *J. Phys. Condens. Matter* **21,** 012208 (2009).
3. Kimber, S. A. J. *et al.* Similarities between structural distortions under pressure and chemical doping in superconducting $BaFe_2As_2$. *Nature Mater.* **8,** 471–475 (2009).
4. Rotter, M., Tegel, M. & Johrendt, D. Superconductivity at 38 K in the iron arsenide $(Ba_{1-x}K_x)Fe_2As_2$. *Phys. Rev. Lett.* **101,** 107006 (2008).
5. Sefat, A. S. *et al.* Superconductivity at 22 K in Co-doped $BaFe_2As_2$ crystals. *Phys. Rev. Lett.* **101,** 117004 (2008).
6. Liu, C. *et al.* K-doping dependence of the Fermi surface of the iron–arsenic $Ba_{1-x}K_xFe_2As_2$ superconductor using angle-resolved photoemission spectroscopy. *Phys. Rev. Lett.* **101,** 177005 (2008).
7. Brouet, V. *et al.* Significant reduction of electronic correlations upon isovalent Ru substitution of $BaFe_2As_2$. *Phys. Rev. Lett.* **105,** 087001 (2010).
8. Ding, H. *et al.* Electronic structure of optimally doped pnictide $Ba_0.6K_0.4Fe_2As_2$: A comprehensive angle-resolved photoemission spectroscopy investigation. *J. Phys. Condens. Matter* **23,** 135701 (2011).
9. Koitzsch, A. *et al.* Temperature and doping-dependent renormalization effects of the low energy electronic structure of $Ba_{1-x}K_xFe_2As_2$ single crystals. *Phys. Rev. Lett.* **102,** 167001 (2009).
10. Fink, J. *et al.* Electronic structure studies of $BaFe_2As_2$ by angle-resolved photoemission spectroscopy. *Phys. Rev. B* **79,** 155118 (2009).
11. Zhang, Y. *et al.* Orbital characters of bands in the iron-based superconductor $BaFe_{1.85}Co_{0.15}As_2$. *Phys. Rev. B* **83,** 054510 (2011).
12. Mansart, B. *et al.* Orbital nature of the hole-like Fermi surface in superconducting $Ba(Fe_{1-x}Co_x)_2As_2$. *Phys. Rev. B* **83,** 064516 (2011).
13. Wen, H-H. & Li, S. Materials and novel superconductivity in iron pnictide superconductors. *Annu. Rev. Condens. Matter Phys.* **2,** 121–140 (2011).
14. Singh, D. J. Electronic structure and doping in $BaFe_2As_2$ and LiFeAs: Density functional calculations. *Phys. Rev. B* **78,** 094511 (2008).
15. Yi, M. *et al.* Electronic structure of the $BaFe_2As_2$ family of iron-pnictide superconductors. *Phys. Rev. B* **80,** 024515 (2009).
16. Brouet, V. *et al.* Orbitally resolved lifetimes in $Ba(Fe_{0.92}Co_{0.08})_2As_2$ measured by ARPES. Preprint at http://arxiv.org/abs/1105.5604 (2011).
17. Ding, H. *et al.* Observation of Fermi-surface-dependent nodeless superconducting gaps in $Ba_{0.6}K_{0.4}Fe_2As_2$. *Europhys. Lett.* **83,** 47001 (2008).
18. Kuroki, K. *et al.* Unconventional pairing originating from disconnected Fermi surfaces in superconducting $LaFeAsO_{1-x}F_x$. *Phys. Rev. Lett.* **101,** 087004 (2008).
19. Onari, S., Kontani, H. & Sato, M. Structure of neutron-scattering peaks in both s++-wave and s++-wave states of an iron pnictide superconductor. *Phys. Rev. B* **81,** 060504(R) (2010).
20. Georges, A., Kotliar, G., Krauth, W. & Rozenberg, M. J. Dynamical mean-field theory of strongly correlated fermion systems and the limit of infinite dimensions. *Rev. Mod. Phys.* **68,** 13–125 (1996).
21. Anisimov, V. I., Poteryaev, A. I., Korotin, M. A., Anokhin, A. O. & Kotliar, G. First-principles calculations of the electronic structure and spectra of strongly correlated systems: Dynamical mean-field theory. *J. Phys. Condens. Matter* **9,** 7359–7367 (1997).
22. Lichtenstein, A. I. & Katsnelson, M. I. *Ab initio* calculations of quasiparticle band structure in correlated systems: LDA++ approach. *Phys. Rev. B* **57,** 6884–6895 (1998).
23. Skornyakov, S. L. *et al.* Classification of the electronic correlation strength in the iron pnictides: The case of the parent compound $BaFe_2As_2$. *Phys. Rev. B* **80,** 092501 (2009).
24. Shim, J. H., Haule, K. & Kotliar, G. Density-functional calculations of the electronic structures and magnetism of the pnictide superconductors $BaFeAs_2$ and $BaFeSb_2$. *Phys. Rev. B* **79,** 060501 (2009).
25. Aichhorn, M. *et al.* Dynamical mean-field theory within an augmented plane-wave framework: Assessing electronic correlations in the iron pnictide LaFeAsO. *Phys. Rev. B* **80,** 085101 (2009).
26. Kutepov, A., Haule, K., Savrasov, S. Y. & Kotliar, G. Self-consistent GW determination of the interaction strength: Application to the iron arsenide superconductors. *Phys. Rev. B* **82,** 045105 (2010).
27. Aryasetiawan, F. *et al.* Frequency-dependent local interactions and low-energy effective models from electronic structure calculations. *Phys. Rev. B* **70,** 195104 (2004).
28. Miyake, T. & Aryasetiawan, F. Screened Coulomb interaction in the maximally localized Wannier basis. *Phys. Rev. B* **77,** 085122 (2008).
29. Yin, Z. P., Haule, K. & Kotliar, G. Magnetism and charge dynamics in iron pnictides. *Nature Phys.* **7,** 294–297 (2011).
30. Werner, P. & Millis, A. J. Efficient DMFT-simulation of the Holstein–Hubbard model. *Phys. Rev. Lett.* **99,** 146404 (2007).

31. Werner, P. & Millis, A. J. Dynamical screening in correlated electron materials. *Phys. Rev. Lett.* **104,** 146401 (2010).
32. Werner, P., Comanac, A., De' Medici, L., Troyer, M. & Millis, A. J. A continuous-time solver for quantum impurity models. *Phys. Rev. Lett.* **97,** 076405 (2006).
33. Casula, M., Rubtsov, A. & Biermann, S. Dynamical screening effects in correlated materials: Plasmon satellites and spectral weight transfers from a Green's function ansatz to extended dynamical mean field theory. *Phys. Rev. B* **85,** 035115 (2012).
34. de Jong, S. *et al*. High-resolution, hard x-ray photoemission investigation of $BaFe_2As_2$: Moderate influence of the surface and evidence for a low degree of Fe3dAs4p hybridization of electronic states near the Fermi energy. *Phys. Rev. B* **79,** 115125 (2009).
35. Werner, P., Gull, E., Troyer, M. & Millis, A. J. Spin freezing transition and non-Fermi-liquid self-energy in a 3-orbital model. *Phys. Rev. Lett.* **101,** 166405 (2008).
36. Haule, K. & Kotliar, G. Coherence–incoherence crossover in the normal state of iron oxypnictides and importance of Hund's rule coupling. *New J. Phys.* **11,** 025021 (2009).
37. Aichhorn, M., Biermann, S., Miyake, T., Georges, A. & Imada, M. Theoretical evidence for strong correlations and incoherent metallic state in FeSe. *Phys. Rev. B* **82,** 064504 (2010).
38. Ishida, H. & Liebsch, A. Fermi-liquid, non-Fermi-liquid, and Mott phases in iron pnictides and cuprates. *Phys. Rev. B* **81,** 054513 (2010).
39. Popovich, P. *et al*. Specific heat measurements of $Ba_{0.68}K_{0.32}Fe_2As_2$ single crystals: Evidence for a multiband strong-coupling superconducting state. *Phys. Rev. Lett.* **105,** 027003 (2010).
40. Andersen, O. K. & Boeri, L. On the multi-orbital band structure and itinerant magnetism of iron-based superconductors. *Ann. Phys.* **523,** 8–50 (2011).
41. Sato, T. *et al*. Band structure and Fermi surface of an extremely overdoped iron-based superconductor KFe_2As_2. *Phys. Rev. Lett.* **103,** 047002 (2009).
42. Yoshida, T. *et al*. Fermi surfaces and quasi-particle band dispersions of the iron pnictides superconductor KFe_2As_2 observed by angle-resolved photoemission spectroscopy. *Proc. 9th International Conference on Spectroscopies in Novel Superconductors* (SNS2010), (2010).
43. Si, Q. & Smith, J. L. Kosterlitz–Thouless transition and short range spatial correlations in an extended Hubbard model. *Phys. Rev. Lett.* **77,** 3391–3394 (1996).
44. Kajueter, H. Ph.D. thesis, Rutgers Univ. (1996).
45. Biermann, S., Aryasetiawan, F. & Georges, A. First-principles approach to the electronic structure of strongly correlated systems: Combining the *GW* approximation and dynamical mean-field theory. *Phys. Rev. Lett.* **90,** 086402 (2003).
46. Albuquerque, A. F. *et al*. The ALPS project release 1.3: Open source software for strongly correlated systems. *J. Magn. Magn. Mater.* **310,** 1187–1193 (2007).

Acknowledgements

We thank M. Aichhorn, H. Aoki, R. Arita, V. Brouet, H. Ding, T. Qian and L. Vaugier for discussions. The DMFT calculations were run on the Brutus cluster at ETH (Eidgenössische Technische Hochschule) Zurich using a code based on ALPS (ref. 46). We thank E. Gull for providing the code for the DMFT-self-consistency loop. This work was supported by the Swiss National Science Foundation (grant PP0022-118866), the G-COE program of the Japanese Ministry of Education, Culture, Sports, Science, and Technology (MEXT; G-03), the French Agence Nationale de la Recherche under project CORRELMAT, Institut du Développement et des Ressources en Informatique Scientifique/Grand Equipement National de Calcul Intensif Orsay under project 20111393 and the US National Science Foundation under grant DMR-1006282. We also acknowledge the hospitality of the Kavli Institute for Theoretical Physics Santa Barbara, where this work was initiated.

Author contributions

S.B. proposed the specific materials project, T.M. provided the LDA Hamiltonian and frequency-dependent interaction, P.W. carried out the DMFT calculations and M.C. did the data analysis (analytical continuation) and produced the figures. P.W. and S.B. wrote the manuscript, with help from the other authors. All authors participated in the planning of the study and the interpretation of the data.

Additional information

The authors declare no competing financial interests. Supplementary information accompanies this paper